International Journal of Nanomedicine

Dovepress
Taylor & Francis Group

Open Access Full Text Article

ORIGINAL RESEARCH

A Dual-Stimuli Responsive Nanoplatform via Atomic Layer Deposition of Gold on $CoFe_2O_4$ for Thermally Gated Doxorubicin Delivery in Colorectal Cancer

Yutian Zhang[1,*], Lang Liu[2,*], Tianlin Wang[3], Ziyi Qu[4], Lei Liang[1], Huizhen Li[3], Hong Wang[5]

[1]Graduate School, Tianjin University of Traditional Chinese Medicine, Tianjin, 300100, People's Republic of China; [2]College of Meteorology and Oceanography, National University of Defense Technology, Changsha, Hunan, 410073, People's Republic of China; [3]Department of Gastroenterology, The Second Affiliated Hospital of Tianjin University of Traditional Chinese Medicine, Tianjin, 300100, People's Republic of China; [4]Department of Nephrology, Shenzhen Traditional Chinese Medicine Hospital, The Fourth Clinical Medical College of Guangzhou University of Chinese Medicine, Shenzhen, Guangdong, People's Republic of China; [5]Department of General Surgery, The Second Affiliated Hospital of Tianjin University of Traditional Chinese Medicine, Tianjin, 300100, People's Republic of China

*These authors contributed equally to this work

Correspondence: Huizhen Li; Hong Wang, Email ctjenny@126.com; ctwanghong@sina.com

Introduction: Targeted chemotherapy for colorectal cancer is often limited by nonspecific drug distribution and systemic toxicity. To improve local therapeutic efficacy and reduce side effects, we designed a thermally gated, dual-stimuli-responsive nanoplatform for controlled doxorubicin (DOX) delivery.

Methods: $CoFe_2O_4$ (CFO) nanocubes were synthesized and coated with Au nanoparticles via atomic layer deposition (ALD) to obtain CFO/Au nanocomposites with enhanced photothermal properties while retaining magnetic responsiveness. The optimal sample (CFO/Au-2) was further modified with poly(acrylic acid) (PAA) to improve aqueous dispersibility and provide abundant carboxyl groups for DOX loading, yielding CFO/Au-2/PAA/DOX. A thermal gate was then constructed using 1-tetradecanol (TD), a phase-change material with a melting point of ~38 °C, to obtain CFO/Au-2/PAA/DOX/TD. The structural, magnetic, and photothermal properties, DOX loading and release behavior, and in vitro cytotoxicity against SW620 colorectal cancer cells were systematically evaluated under near-infrared (NIR) irradiation and/or alternating magnetic field (AMF).

Results: CFO/Au-2/PAA/DOX/TD exhibited a high DOX loading capacity (~26 wt%) and good colloidal stability. Minimal DOX leakage occurred at physiological temperature, confirming effective encapsulation by solid TD. Under NIR and/or AMF stimulation, the nanocomposite generated pronounced local heating, induced TD melting, and triggered rapid DOX release, with the combined NIR + AMF condition producing the fastest release profile. In vitro, the carrier without DOX showed minimal cytotoxicity toward SW620 cells, whereas CFO/Au-2/PAA/DOX/TD under dual stimulation produced significantly enhanced cytotoxicity toward SW620 cells compared with free DOX at the same drug concentration.

Conclusion: This ALD-engineered CFO/Au-2/PAA/DOX/TD nanoplatform integrates magnetic and photothermal heating with thermally gated, dual-stimuli-responsive drug release, enabling precise spatiotemporal control of DOX delivery. The results suggest strong potential for combined and localized colorectal cancer therapy with reduced systemic toxicity.

Keywords: colorectal cancer, $CoFe_2O_4$ nanocubes, atomic layer deposition, doxorubicin delivery, photothermal therapy, phase-change material

Introduction

Colorectal cancer (CRC) has been a leading cause of cancer-related mortality, underscoring the urgent need for more effective and targeted therapeutic strategies.[1–3] Chemotherapy, particularly with agents such as doxorubicin (DOX), remains a cornerstone of treatment.[4–7] However, its clinical application is frequently limited by systemic toxicity, non-

https://doi.org/10.2147/IJN.S563711
Received: 28 August 2025
Accepted: 10 December 2025
Published: 4 February 2026

specific biodistribution, and poor tumor-site accumulation. To overcome these limitations, nanocarrier-based drug delivery systems have become a promising method to improve the therapeutic index of chemotherapeutics by enhancing their solubility, circulation time, and targeted release.[8,9]

Magnetic nanomaterials, especially cobalt ferrite ($CoFe_2O_4$, CFO), have attracted growing interest in biomedical applications due to their strong magnetic response, high chemical stability, and potential for magnetic field-guided delivery.[10] However, for effective cancer therapy, the integration of additional functionalities such as photothermal activity and controlled drug release mechanisms is essential. Gold (Au) nanoparticles, known for their excellent photothermal conversion efficiency and biocompatibility, can be introduced onto CFO surfaces to generate multifunctional hybrid nanostructures.[11] Atomic layer deposition (ALD) offers a precise and uniform strategy to coat CFO nanocubes with a tunable amount of Au, forming core–shell CFO/Au nanocomposites with tailored magnetic and optical properties.[12–14]

To further improve the aqueous dispersibility and drug loading capability of these nanocomposites, surface modification with poly(acrylic acid) (PAA) was employed.[15] PAA is a hydrophilic polymer widely used for nanoparticle functionalization due to its abundance of carboxylic acid groups, which promote colloidal stability and enable strong binding with drug molecules via hydrogen bonding or electrostatic interactions.[16,17]

In this study, DOX was loaded onto CFO/Au/PAA nanocomposites and sealed using a thermal gate composed of 1-tetradecanol (TD), a phase change material with a melting point around 38 °C.[18,19] Phase-change materials (PCMs) are widely used as thermal gates for on-demand drug release, with common examples including fatty acids, paraffin-type hydrocarbons, PEG-based PCMs, and long-chain fatty alcohols.[19,20] Their melting behavior determines their suitability for biomedical use. Fatty acids and paraffins typically melt above 50–60 °C, making them unsuitable for mild hyperthermia-triggered release,[21] while Polyethylene Glycol (PEG) based PCMs often exhibit broad, less-defined transitions.[22] In contrast, long-chain fatty alcohols such as TD possess a sharp, reversible melting point around 38 °C[18]—just above physiological temperature—allowing precise thermal gating under mild NIR or AMF-induced heating while remaining solid and leakage-resistant at 37 °C. These features motivated the choice of TD as the phase-change component in this work. TD remains solid under physiological conditions, effectively preventing premature drug leakage. Upon application of external stimuli such as near-infrared (NIR) irradiation and/or alternating magnetic field (AMF), the local temperature of the nanocomposite exceeds the melting point of TD, triggering the transition from solid to liquid and thereby enabling controlled DOX release.[23–26] This dual-stimuli responsive system offers precise spatiotemporal control over drug delivery, reducing off-target effects and increasing therapeutic efficacy.

Numerous dual-stimuli (NIR/AMF) responsive nanocarriers have been explored, and most rely on wet-chemical approaches to decorate magnetic nanoparticles with gold. Recent examples include gold-coated magnetic nanoparticles, Fe_3O_4/Au nanocomposites, Janus Au–Fe_3O_4 structures, and polydopamine-coated magnetic nanoclusters,[27–29] all of which demonstrate enhanced heating under simultaneous magnetic and photothermal excitation. However, these synthetic routes typically yield Au nanoparticles with broad size distributions and uneven surface coverage, resulting in inconsistent photothermal performance and suboptimal magnetic heating.[30,31] This lack of structural control makes it difficult to finely tune or systematically optimize dual-mode hyperthermia.

In contrast, the present work employs ALD to introduce Au onto $CoFe_2O_4$ nanocubes with cycle-controlled precision. ALD enables atomic-level control over nucleation and growth, producing exceptionally uniform and reproducible Au coatings with tunable loading.[12,14,32] Such precise, layer-by-layer deposition is highly advantageous for modulating both photothermal conversion efficiency and AMF-induced thermal output, thereby improving the synergistic magneto-photothermal response. Despite these benefits, ALD has rarely been applied in the design of multimodal therapeutic nanoplatforms. Here, we demonstrate ALD-engineered Au/CFO nanocubes as a robust and controllable platform that delivers a highly reproducible NIR–AMF dual-mode heating effect and uniquely enables thermally gated doxorubicin release.

Herein, we report a multifunctional nanoplatform for colorectal cancer therapy, featuring ALD-synthesized Au-coated CFO nanocubes—a highly precise and scalable strategy not commonly applied to magnetic drug-delivery systems. By integrating PAA functionalization for enhanced dispersibility, high-efficiency DOX loading, and thermally gated encapsulation using TD, the system enables on-demand, stimulus-responsive drug release. Under NIR

irradiation and alternating magnetic field (AMF), the nanoplatform achieves combined photothermal and magnetothermal activation, offering spatiotemporal control over drug release. The structural, magnetic, and photothermal properties, together with in vitro cytotoxicity, were thoroughly characterized. This innovative approach, combining ALD precision, phase-change thermal gating, and dual-stimuli responsiveness, demonstrates excellent drug loading, and significantly enhanced therapeutic efficacy—highlighting its strong potential for localized and controlled cancer therapy.

Experiments

Materials

Cobalt(II) acetylacetonate ($Co(acac)_2$, 97%) and iron(III) acetylacetonate ($Fe(acac)_3$, 97%), both purchased from Sigma-Aldrich, were used as metal precursors for the thermal decomposition synthesis of $CoFe_2O_4$ nanocubes. Oleic acid (technical grade, 90%), oleylamine (technical grade, 70%), 1,2-hexadecanediol (≥90%), and benzyl ether (≥98%)—all acquired from Sigma-Aldrich—served as surfactants, solvents, and reducing agents to assist anisotropic crystal growth. For ALD of Au nanoparticles, hydrogen tetrachloroaurate(III) trihydrate ($HAuCl_4 \cdot 3H_2O$, ≥99.9% trace metals basis, Sigma-Aldrich) was used as the Au precursor, while H_2 plasma acted as the reducing agent. PAA (Mw ~1800, 25 wt% solution in water, ≥99% purity, TCI Chemicals) was employed for surface modification to enhance hydrophilicity and drug-binding efficiency. DOX (≥98% HPLC purity, TCI Chemicals) was loaded as a model anticancer drug, and 1-tetradecanol (TD, ≥98%, Alfa Aesar) was used as a thermal-responsive phase change material to enable temperature-controlled drug release. Analytical-grade ethanol and hexane (Fisher Scientific) were utilized for washing steps during purification processes. Phosphate-buffered saline (PBS, pH 7.4, Thermo Fisher) was prepared for in vitro release experiments. For biological assays, RPMI-1640 medium (Gibco), fetal bovine serum (FBS, Gibco), and penicillin–streptomycin (Gibco) were used for culturing SW620 cells, while the MTT reagent (Sigma-Aldrich) was employed to assess cell viability. Ultrapure water with a resistivity of 18.2 MΩ·cm (Milli-Q system) was used throughout all synthesis and characterization steps.

Synthesis of CFO Nanocubes

CFO nanocubes were synthesized through a thermal decomposition method using metal acetylacetonate precursors.[33] Specifically, stoichiometric amounts of cobalt(II) acetylacetonate and iron(III) acetylacetonate were dissolved in a mixture of oleic acid, oleylamine, 1,2-hexadecanediol, and benzyl ether under an inert nitrogen atmosphere. The solution was first degassed at ~110 °C to remove moisture and oxygen, followed by gradual heating to ~200 °C to initiate nucleation. The resultant was then ramped to ~300 °C and maintained for 45 minutes to allow for anisotropic growth and crystal maturation. After cooling to room temperature, the product was washed several times with ethanol and hexane to remove unreacted precursors and surfactants.

Atomic Layer Deposition of Au Nanoparticles on CFO

Au nanoparticles were deposited on CFO nanocubes using a thermal ALD system. $HAuCl_4$ and H_2 plasma were used as the precursor and reducing agent, respectively. The number of ALD cycles was varied to obtain samples with different Au contents, denoted as CFO/Au-1, CFO/Au-2, and CFO/Au-3. The deposition was conducted at 150 °C with a pulse-purge sequence optimized for conformal coating. The key process parameters for ALD deposition are summarized in Table 1.

Surface Modification with PAA

To improve colloidal stability and drug-binding capability, CFO/Au-2 was coated with PAA. Fifty milligrams of CFO/Au-2 was dispersed in 20 mL of water containing 0.5 wt% PAA. The resultant was sonicated and mechanically stirred at room temperature for 12 h. The PAA-modified composite (CFO/Au-2/PAA) was collected by centrifugation and washed to remove excess polymer.

Table 1 Key Process Parameters for the Au ALD Deposition

Parameter	Condition/Value
Substrate	CFO nanocubes
Deposition temperature	150 °C
Au precursor	$HAuCl_4$
Reducing agent	H_2 plasma
Carrier/purge gas	N_2
Step 1: Au precursor pulse	3 seconds
Step 2: N_2 purge	20 seconds
Step 3: H_2 plasma	4 seconds
Step 4: N_2 purge	20 seconds
CFO/Au-1 deposition cycles	50
CFO/Au-2 deposition cycles	100
CFO/Au-3 deposition cycles	150

DOX Loading

DOX was loaded onto CFO/Au-2/PAA via incubation. Ten milligrams of CFO/Au-2/PAA was suspended in 10 mL of DOX aqueous solutions at various concentrations (10–50 μg/mL) and incubated for 24 h in the dark under gentle shaking. The drug-loaded nanocomposite (CFO/Au-2/PAA/DOX) was separated by centrifugation. The amount of loaded DOX was quantified via UV–Vis absorbance at 480 nm using a calibration curve. For the preparation of the final CFO/Au-2/PAA/DOX/TD nanocomposite used in all release and cytotoxicity studies, an initial DOX concentration of 50 μg/mL was employed, corresponding to the saturation loading level (~26 wt%).

Thermal-Gated DOX Release Strategy

To prepare the thermally gated system (denoted as CFO/Au-2/PAA/DOX/TD), 10 mg of DOX-loaded CFO/Au-2/PAA was mixed with 50 mg of molten TD at 45 °C under gentle stirring for 30 minutes to ensure uniform coating. The mixture was then rapidly cooled to room temperature to solidify TD on the nanoparticle surfaces. The resulting solid composite was washed with cold ethanol to remove any unbound TD and stored at 4 °C until use. For the preparation of the final CFO/Au-2/PAA/DOX/TD nanocomposite used in all release and cytotoxicity studies, an initial DOX concentration of 50 μg/mL was employed, corresponding to the saturation loading level (~26 wt%).

Characterization

The morphology and microstructure of the synthesized nanoparticles were examined using transmission electron microscopy (TEM), high-resolution TEM (HRTEM), and selected area electron diffraction (SAED) with a JEOL JEM-2100F. The crystalline structure and phase composition were determined by powder X-ray diffraction (XRD) using a Rigaku SmartLab diffractometer equipped with Cu Kα radiation (λ = 1.5406 Å). Specific surface area and porosity were analyzed through nitrogen adsorption–desorption isotherms measured at 77 K on a Micromeritics ASAP 2020 instrument using the Brunauer–Emmett–Teller (BET) method. Surface chemical composition and oxidation states of the elements were studied using X-ray photoelectron spectroscopy (XPS) on a Thermo Scientific ESCALAB 250Xi system with Al Kα radiation.

Fourier-transform infrared spectroscopy (FT-IR) was performed on a Bruker Tensor 27 spectrometer in the range of 4000–500 cm^{-1} to confirm surface modification with PAA. Magnetic properties of the nanocomposites were evaluated using a Lakeshore 7407 vibrating sample magnetometer (VSM) at room temperature under an applied magnetic field of ±40 kOe. Ultraviolet–visible (UV–Vis) absorption spectra were recorded using a Shimadzu UV-2600 spectrophotometer for the quantitative analysis of DOX loading. Photothermal performance was assessed by dispersing the samples (1 mg/mL) in water and irradiating them with an 808 nm laser (8 W) and/or an alternating magnetic field (AMF, 600 Hz). The temperature rise was recorded in real time using a thermocouple probe.

The phase-transition behavior of TD in the free state and in the CFO/Au-2/PAA/DOX/TD nanocomposite was investigated by differential scanning calorimetry (DSC Q2000, TA Instruments, USA). Approximately 5–8 mg of each sample (pure TD or freeze-dried CFO/Au-2/PAA/DOX/TD) was accurately weighed into an aluminum pan and hermetically sealed; an empty sealed pan was used as the reference. Measurements were performed under a nitrogen atmosphere (50 mL/min) over the temperature range of 20–60 °C at a heating/cooling rate of 10 °C/min. Two consecutive heating–cooling cycles were recorded for each sample to evaluate the reproducibility of the phase transition. The melting temperature (T_m) and associated enthalpy (ΔH) of TD were determined from the endothermic peak in the second heating scan for both pure TD and the nanocomposite.

Vitro DOX Release

To study the drug release behavior of the nanocomposites, DOX-loaded CFO/Au-2/PAA/DOX/TD was placed in a dialysis bag (molecular weight cut-off ~12 kDa) and immersed in 20 mL of PBS under constant agitation at 100 rpm. Unless otherwise noted, the environment temperature is 22 °C for all experimental conditions in this study. The release kinetics were studied under various temperatures (35 °C, 37 °C, 39 °C, 41 °C, and 43 °C), as well as under external stimuli including AMF (600 Hz), NIR laser irradiation (808 nm, 8 W), and the combination of both. At predetermined time intervals, 1 mL aliquots of the release medium were collected and replaced with an equal volume of fresh PBS. The cumulative DOX concentration in the release medium was quantified using UV–Vis spectroscopy by measuring the absorbance at 480 nm, and the results were expressed as cumulative percentage of DOX released over time.

Cell Viability Assay

The cytotoxicity and therapeutic performance of the synthesized nanocomposites were assessed using SW620 human colorectal cancer cells, sourced from the Cell Bank of the Chinese Academy of Sciences (Shanghai, China). Cells were maintained in RPMI-1640 medium supplemented with 10% FBS and 1% penicillin–streptomycin at 37 °C in a 5% CO_2 humidified incubator. For cytotoxicity evaluation, cells were seeded at a density of 1×10^4 cells per well in 96-well plates and incubated for 24 hours prior to treatment with varying concentrations (0–100 μg/mL) of CFO/Au-2/PAA/TD. After an additional 24-hour exposure, cell viability was determined via the MTT (3-(4,5-dimethylthiazol-2-yl)-2,5-diphenyl tetrazolium bromide) assay by measuring absorbance at 570 nm. For therapeutic efficacy analysis, cells were treated with either free DOX or DOX-loaded nanocomposites (0.1–4 μg/mL DOX-equivalent) and subjected to 5 minutes of NIR and/or AMF stimulation. Post-treatment viability was evaluated after a 24-hour incubation, with results expressed relative to untreated controls. Specifically, all drug-release experiments, DOX-loading measurements, and cell-viability assays were performed in triplicate ($n = 3$) unless otherwise noted. The corresponding figures display mean ± standard deviation (SD) with appropriate error bars. Statistical significance was evaluated by one-way ANOVA ($p < 0.05$).

Results and Discussion

The morphology and structure of the synthesized $CoFe_2O_4$ (CFO) and CFO/Au nanocomposites were examined using TEM, as shown in Figure 1.

Figure 1a displays the TEM image of pristine CFO nanocubes, which are monodisperse with a uniform cubic morphology and an average edge length of approximately 20 nm. The corresponding HRTEM image (Figure 1b) reveals well-resolved lattice fringes, a signature for high crystallinity. The SAED patterns (Figure 1c) exhibit distinct diffraction rings corresponding to the spinel structure of CFO, confirming its polycrystalline nature.

Upon deposition of Au nanoparticles via ALD, the composite CFO/Au-2 exhibits a similar cubic morphology (Figure 1d), but with a visible contrast variation at the surface, suggesting the successful deposition of Au. The HRTEM image (Figure 1e) further confirms the formation of a conformal Au layer around the CFO core, as evidenced by the presence of additional lattice fringes at the particle edges. A line scan elemental profile (Figure 1f) across a single particle reveals a core–shell distribution, where Fe (black) is dominant in the core and Au (red) is enriched near the surface, further confirming the core@shell structure of CFO/Au-2.

https://doi.org/10.2147/IJN.S563711

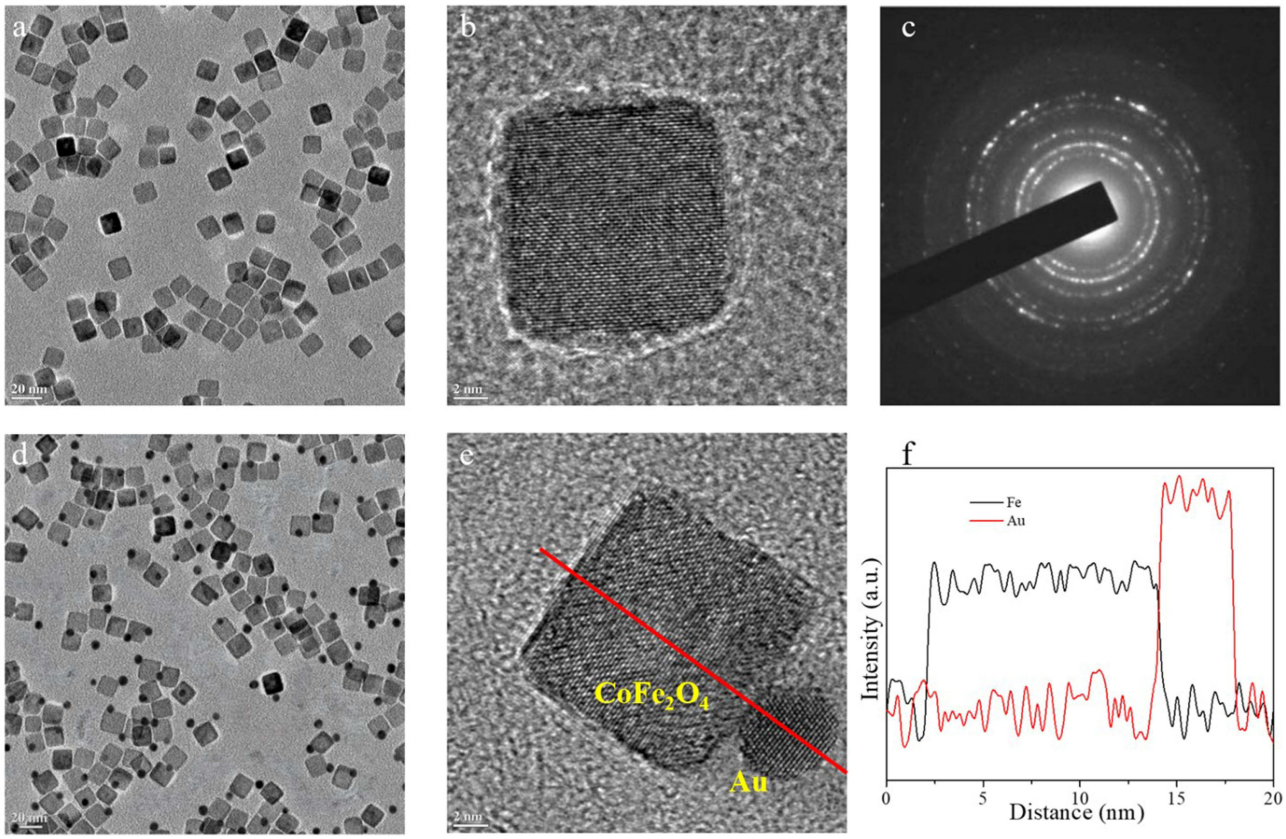

Figure 1 (**a–c**) TEM, High-resolution TEM, TEM diffraction patterns for CFO; (**d–f**) TEM, high-resolution TEM (red line shows elemental line scan position c), and elemental line scan profile for CFO/Au-2.

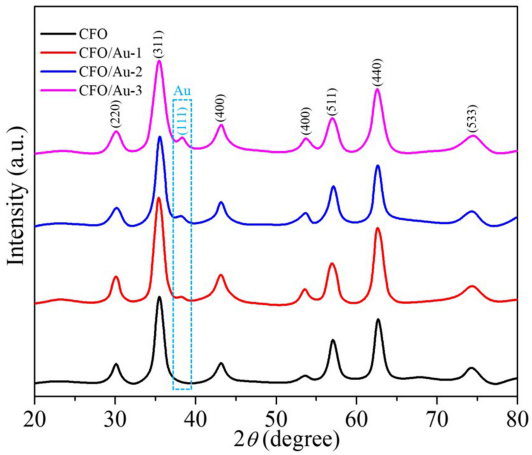

Figure 2 Powder XRD patterns for CFO, CFO/Au-1, CFO/Au-2, and CFO/Au-3.

These results demonstrate the successful and uniform deposition of Au onto CFO nanocubes via ALD, forming a well-defined core–shell structure that is expected to enhance drug delivery efficiency through improved surface functionality and potential photothermal effects.

The crystalline structure of CFO and CFO/Au composites was analyzed via powder XRD, as shown in Figure 2. The peaks of pristine CFO match well with the standard spinel phase of $CoFe_2O_4$ (JCPDS No. 22–1086), confirming the successful synthesis of pure CFO nanocubes. Upon Au nanoparticle deposition, additional peak emerges at around 38.2°,

https://doi.org/10.2147/IJN.S563711

which correspond to the (111) plane of face-centered cubic (fcc) Au (JCPDS No. 04–0784) in CFO/Au-1. These peaks become more pronounced with increasing Au content from CFO/Au-2 to CFO/Au-3, confirming the successful loading of Au nanoparticles. The intensity of Au-related peaks correlates with the increasing Au concentration, indicating a tunable degree of Au deposition via ALD.[32]

Notably, the CFO diffraction peaks remain unchanged in position and shape after Au coating, suggesting that the spinel structure of CFO is retained and that the ALD process does not alter the bulk crystallinity of the core material. This structural integrity, combined with the surface modification from Au, provides a stable platform for drug loading and potential combined effects in colorectal cancer therapy.

The specific surface area and porosity characteristics of CFO and CFO/Au composites were evaluated using nitrogen adsorption–desorption isotherms, as shown in Figure 3a–d. All samples exhibit typical type IV isotherms with distinct H3-type hysteresis loops in the relative pressure range of 0.7–1.0, indicating mesoporous structures.

The isotherms of CFO (Figure 3a), CFO/Au-1 (Figure 3b), CFO/Au-2 (Figure 3c), and CFO/Au-3 (Figure 3d) show nearly identical profiles, suggesting that the introduction of Au nanoparticles via ALD has negligible influence on the overall surface area and porosity of the composites. The similarity in adsorption capacity and hysteresis behavior across all samples indicates that the mesoporous framework of the CFO nanocubes remains intact after Au deposition. This structural stability is advantageous for drug delivery applications, as it ensures consistent surface area for drug loading and release, while the presence of Au enhances surface functionality without compromising the intrinsic porosity of the material.

XPS was conducted to study the surface elemental composition and oxidation states of the CFO and CFO/Au composites. Figure 4a–c displays the high-resolution spectra for Co 2p, Fe 2p, and Au 4f regions, respectively.

In the Co 2p region (Figure 4a), two prominent peaks centered around 780 eV and 796 eV are attributed to Co^{2+} $2p_{3/2}$ and Co^{2+} $2p_{1/2}$, respectively. Similarly, in the Fe 2p region (Figure 4b), the peaks at ~711 eV and ~724 eV refer to Fe^{3+}

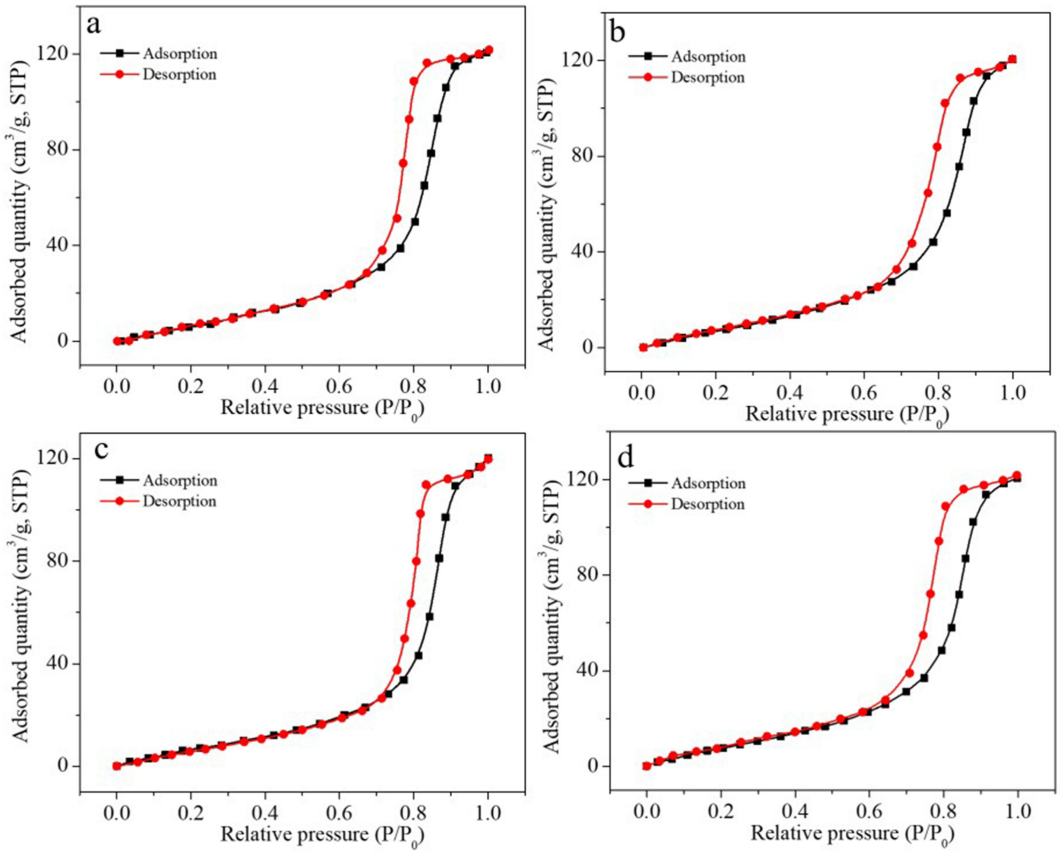

Figure 3 (**a–d**) nitrogen adsorption-desorption isotherms of CFO, CFO/Au-1, CFO/Au-2, and CFO/Au-3 (Adsorbed quantity presented as cm^3/g (STP) for all samples).

https://doi.org/10.2147/IJN.S563711

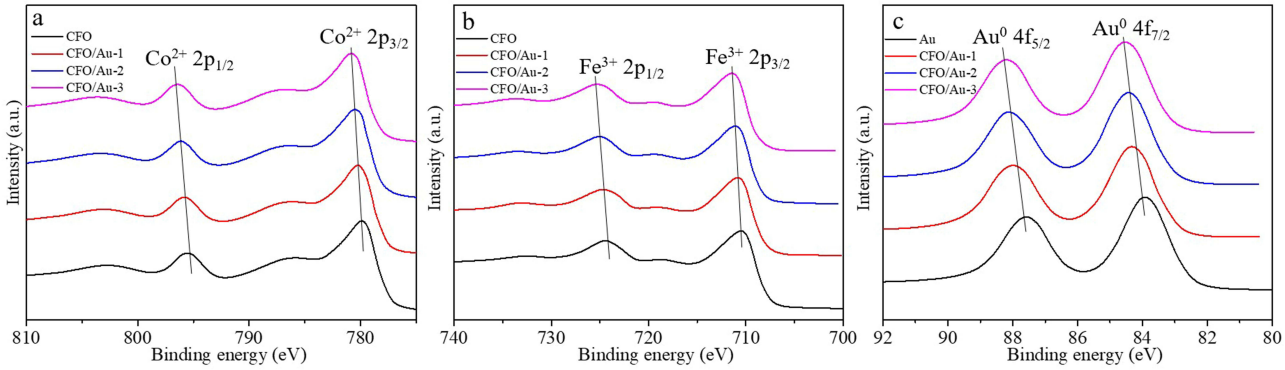

Figure 4 High-resolution XPS for (**a**) Co2+ and (**b**) Fe3+ CFO, CFO/Au-1, CFO/Au-2, and CFO/Au-3; high-resolution XPS for (**c**) Au0 in Au, CFO/Au-1, CFO/Au-2, and CFO/Au-3.

$2p_{3/2}$ and Fe^{3+} $2p_{1/2}$. These characteristic peaks are clearly observed in all samples and show no significant shift after Au deposition, indicating that the spinel structure of CFO is preserved and the core metal oxidation states remain stable throughout the ALD process.[34]

The successful incorporation of metallic gold is confirmed by the Au 4f spectrum (Figure 4c). CFO/Au-1, CFO/Au-2, and CFO/Au-3 display clear peaks at ~84.0 eV and ~87.7 eV, which are attributed to Au^0 $4f_{7/2}$ and Au^0 $4f_{5/2}$, respectively. These binding energies are consistent with metallic gold, suggesting that the Au nanoparticles deposited on the CFO surface retain their zero-valent state. As expected, the intensity of the Au peaks increases proportionally with Au loading, from CFO/Au-1 to CFO/Au-3, indicating the controlled and tunable deposition of Au via atomic layer deposition.

These results validate the successful surface modification of CFO nanocubes with metallic Au while maintaining the integrity of the core composition and structure, which is crucial for maintaining magnetic properties and achieving multifunctionality in drug delivery systems.

The starting CFO mass for ALD deposition is 0.1 g. After the 50, 100, and 150 ALD cycles, the mass increases to 0.1075, 0.1153, and 0.1217 g, corresponding to Au mass fractions of 7.0 wt%, 13.3 wt%, and 17.8 wt% for CFO/Au-1, CFO/Au-2, and CFO/Au-3, respectively. To assess the combined thermal conversion capabilities of the nanocomposites, the temperature evolution of aqueous suspensions of CFO, CFO/Au-1, CFO/Au-2, and CFO/Au-3 was monitored under combined alternating magnetic field (AMF, 600 Hz) and NIR (8 W) irradiation, as shown in Figure 5. Pure water served as a control and showed negligible temperature increase, confirming that the heating originates from the nanomaterials.

Among all samples, CFO/Au-2 exhibited the most pronounced temperature increase, reaching ~30 °C above baseline within 600 seconds. This enhancement is attributed to the optimized combination of CFO and Au shell. The thermal

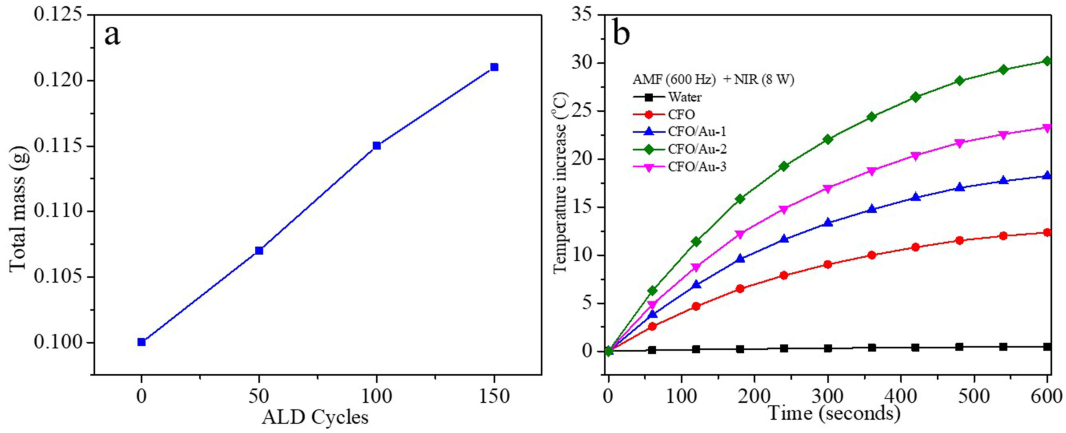

Figure 5 (**a**) Sample total mass after ALD cycles; (**b**) temperature change of water and CFO/Au-1, CFO/Au-2, and CFO/Au-3 aqueous suspension under AFM and NIR irradiation.

https://doi.org/10.2147/IJN.S563711

output increases with Au loading from CFO to CFO/Au-2, but slightly declines for CFO/Au-3, likely due to excessive Au shielding the magnetic response of the CFO core, thereby reducing AMF-induced heating efficiency.

This result suggests that CFO/Au-2 possesses the optimal balance between magnetic and plasmonic components, enabling effective dual-mode hyperthermia. Such performance is highly desirable for cancer therapy applications, where localized heating can promote drug release and enhance cytotoxic effects without damaging surrounding healthy tissues.

FT-IR spectroscopy was employed to study the surface functionalization of CFO/Au-2 with poly(acrylic acid) (PAA), as shown in Figure 6. The spectrum of pure PAA displays characteristic bands at 3448 cm^{-1} (O–H stretching), 2952 cm^{-1} (C–H stretching), 1727 cm^{-1} (C=O stretching of carboxylic acid), and 1456 cm^{-1} (C–H bending), confirming the presence of carboxylic functional groups.[35]

The FT-IR spectrum of CFO/Au-2 (red) reveals a strong band at 602 cm^{-1}, which refers to the Fe–O stretching vibration of the spinel $CoFe_2O_4$ structure.[36] This signature remains present after PAA coating, indicating the structural integrity of the magnetic core.

In the CFO/Au-2/PAA composite (blue), the characteristic PAA peaks at 1727 cm^{-1} and 1456 cm^{-1} are clearly visible, confirming the successful surface functionalization of the nanocomposite with PAA. The broad O–H band at ~3448 cm^{-1} is also retained, which may contribute to improved hydrophilicity and colloidal stability.

This polymer coating not only enhances the water dispersibility of the composite but also introduces abundant –COOH groups that can effectively bind with doxorubicin (DOX) via hydrogen bonding or electrostatic interactions, thereby improving drug-loading efficiency.[37]

To evaluate the drug delivery capability of the prepared nanocomposites, UV–Vis absorption spectroscopy, drug loading measurements, and magnetic hysteresis analysis were performed, as shown in Figure 7.

Figure 7a displays the UV–Vis spectra of pure DOX, CFO/Au-2/PAA, and DOX-loaded CFO/Au-2/PAA (denoted CFO/Au-2/PAA/DOX/TD). The strong absorption band of DOX at ~480 nm is clearly observed in the spectrum of the DOX-loaded composite, indicating the successful loading of DOX into the nanocarrier. The composite alone (black curve) shows negligible absorption in this region, eliminating interference from the carrier.

Magnetic hysteresis loops of CFO/Au-2, CFO/Au-2/PAA, and CFO/Au-2/PAA/DOX/TD were measured to assess their magnetic response, as shown in Figure 7b. All samples exhibit typical soft ferromagnetic behavior. The saturation magnetization (Ms) decreases slightly after PAA coating and DOX loading, due to the non-magnetic nature of the polymer and drug molecules. Nevertheless, CFO/Au-2/PAA/DOX/TD retains sufficient magnetic response for potential magnetic guidance and separation in biomedical applications. These results confirm that CFO/Au-2/PAA retains its magnetic manipulability after DOX loading, offering multifunctionality for targeted cancer therapy. To be brief, the key physical parameter summary for CFO, CFO/Au-1, CFO/Au-2, and CFO/Au-3 is presented in Table 2.

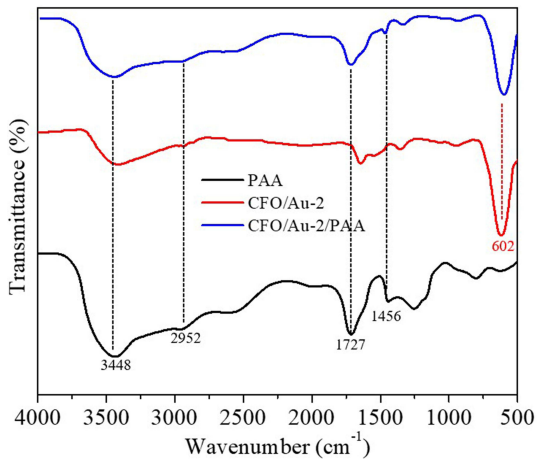

Figure 6 FT-IR spectra for PAA, CFO/Au-2, and CFO/Au-2/PAA.

https://doi.org/10.2147/IJN.S563711

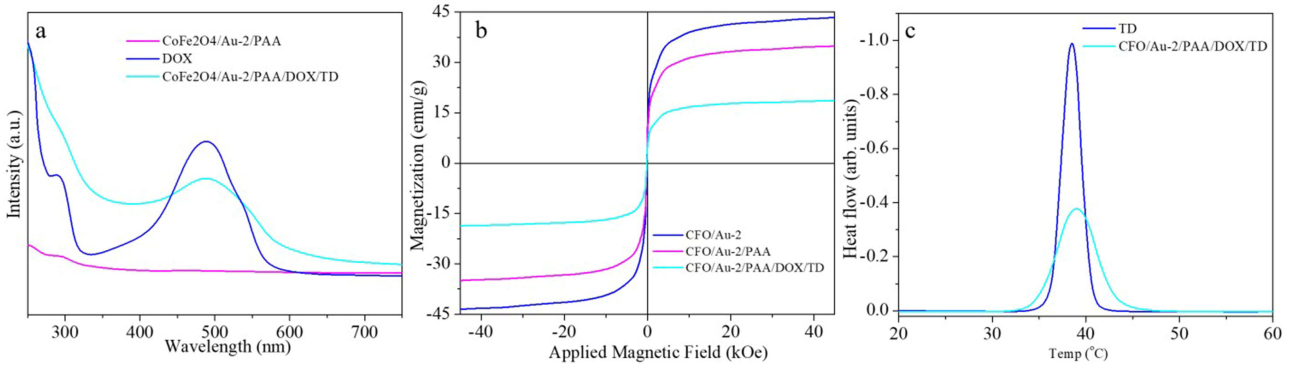

Figure 7 (**a**) UV-Vis spectra of CFO/Au-2/PAA, DOX, and CFO/Au-2/PAA/DOX/TD; (**b**) DOX loading capacity of CFO/Au-2/PAA; (**c**) Magnetic hysteresis loops of CFO/Au-2, CFO/Au-2/PAA, and CFO/Au-2/PAA/DOX/TD.

The thermosensitive behaviour of TD in the nanocomposite was further verified by DSC in Figure 7c. Pure TD displays a single, sharp endothermic peak centred at ~38–39 °C, characteristic of its solid–liquid melting transition. A similar endothermic peak appears in the CFO/Au-2/PAA/DOX/TD sample in the same temperature region, indicating that TD preserves its intrinsic phase-transition behaviour after being coated on the CFO/Au-2/PAA/DOX surface. The peak observed for pure TD is higher and narrower because the entire sample consists of bulk TD crystals that melt within a very narrow temperature interval, giving a large enthalpy change per gram. In contrast, TD accounts for only a fraction of the mass in the CFO/Au-2/PAA/DOX/TD composite and is distributed as a confined coating around the nanoparticles, so the effective enthalpy per gram of composite is lower and the local environments of TD are more heterogeneous; consequently, the melting peak is reduced in intensity and broadened.

Structural characterization was performed for CFO and CFO/Au-2 to confirm that the ALD process and subsequent PAA coating do not alter the crystalline structure of the $CoFe_2O_4$ core (XRD) or morphology (TEM). The final drug-loaded and TD-coated CFO/Au-2/PAA/DOX/TD formulation was not subjected to additional XRD or TEM analysis due to the amorphous nature of TD and the low contrast of the organic coatings, but future work will include elemental mapping and imaging to visualize the complete multilayer structure.

As shown in Figure 8a, PAA-functionalized CFO/Au-2/PAA exhibits a much higher loading capacity that increases with DOX concentration and plateaus at ~26 w/w% at an initial DOX concentration of 50 μg mL^{-1}. In sharp contrast, the maximum loading capacity of CFO/Au-2 without PAA is only ~3 w/w% in the same concentration range (Figure 8b). This nearly one-order-of-magnitude enhancement directly demonstrates that the PAA shell, with its abundant –COOH groups, is crucial for strengthening DOX binding on the nanocomposite surface.[38] Unless otherwise noted, all DOX release and cytotoxicity experiments were conducted using the CFO/Au-2/PAA/DOX/TD composite prepared at an initial DOX concentration of 50 μg/mL, which yields a loading capacity of ~26 wt%.

The high DOX loading (~26 wt%) observed for CFO/Au-2/PAA is largely attributed to the PAA coating, which introduces abundant surface –COOH groups capable of forming strong electrostatic and hydrogen-bond interactions with DOX molecules.[38] The BET results indicate that the surface area of the nanocomposites is moderate and typical of

Table 2 Key Physical Parameter Summary for CFO, CFO/Au-1, CFO/Au-2, and CFO/Au-3

Parameter	CFO	CFO/Au-1	CFO/Au-2	CFO/Au-3
Size	~20 nm	~20/4 nm	~20/4 nm	~20/4 nm
BET surface area	56.3 m^2/g	54.7 m^2/g	52.4 m^2/g	49.8 m^2/g
ALD cycle	0	50	100	150
Au mass percent	0	7.0 wt%	13.3 wt%	17.8 wt%
Saturation magnetization	50.2 emu/g	45.8 emu/g	43.6 emu/g	40.5 emu/g

 https://doi.org/10.2147/IJN.S563711

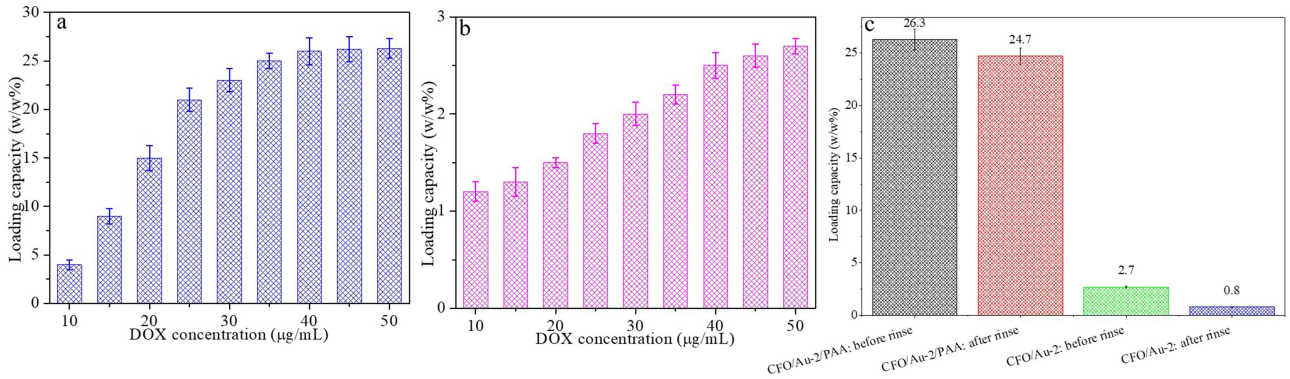

Figure 8 (**a**) DOX loading capacity of CFO/Au-2 as a function of initial DOX concentration. (**b**) DOX loading capacity of CFO/Au-2/PAA as a function of initial DOX concentration; (**c**) the DOX loading of CFO/Au-2/DOX and CFO/Au-2/PAA after 5 rinse cycles.

nanoparticle assemblies. Thus, porosity likely plays only a secondary role in drug adsorption compared to the PAA-mediated binding affinity.

The stability of the PAA–DOX layer was further evaluated by repeated washing (five rinse cycles; Figure 8c). For CFO/Au-2/PAA, the loading capacity decreases only slightly from 26.3 to 24.7 w/w% after rinsing, retaining ~94% of the initially bound DOX, which demonstrates that most DOX molecules are firmly anchored to the PAA shell. In sharp contrast, CFO/Au-2 without PAA loses the majority of its loaded DOX under the same treatment: the loading capacity drops from 2.7 to 0.8 w/w%, corresponding to only ~30% retention. These results clearly show that PAA not only enables high DOX uptake but also significantly improves the binding stability, providing a robust and leakage-resistant drug reservoir on the nanocomposite surface.

The release behavior of DOX from CFO/Au-2/PAA/DOX/TD nanocomposites was studied under various thermal and external stimulus conditions, as illustrated in Figure 8.

Figure 9a shows the cumulative DOX release profiles at different ambient temperatures ranging from 35 °C to 43 °C. The release rate exhibits a strong temperature dependence, with negligible release observed at physiological temperature (37 °C), indicating high drug retention under normal conditions. In contrast, elevated temperatures (≥ 39 °C) significantly accelerate DOX release, with the release efficiency reaching ~95% within 24 hours at 43 °C. Notably, the onset of this endothermic transition (~38 °C) agrees well with the temperature at which the TD phase transition temperature show in Figure 7C, confirming that TD acts as a thermosensitive switch that modulates drug leakage through its reversible solid–liquid phase transition.

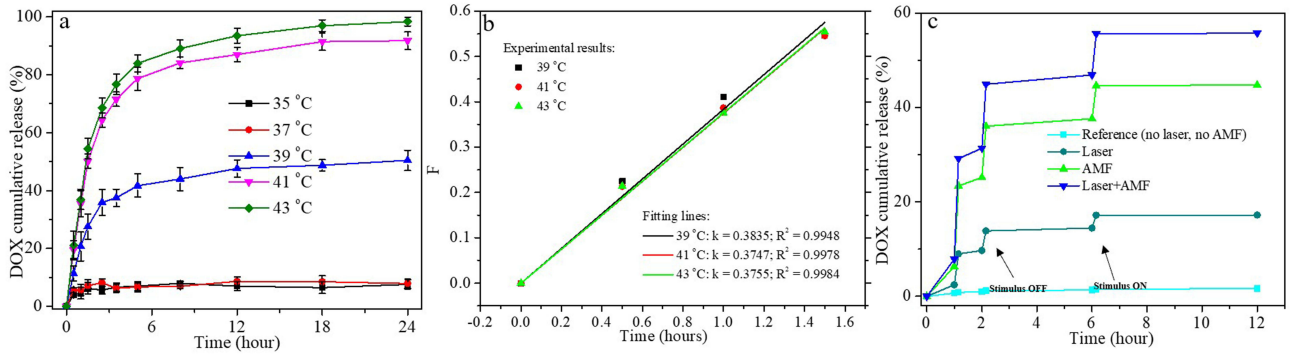

Figure 9 (**a**) Cumulative release profiles of DOX from CFO/Au-2/PAA/DOX/TD at various ambient temperatures; (**b**) Zero-order kinetic fitting of DOX release from CFO/Au-2/PAA/DOX/TD at different temperatures. Symbols represent the experimental fractional release F=Mt/M∞ (0–60% of equilibrium release) at 39 °C (squares), 41 °C (circles), and 43 °C (triangles). Solid lines are linear fits according to the zero-order model F = kt; (**c**) Cumulative DOX release triggered by NIR irradiation, AMF exposure, and their combined application.

https://doi.org/10.2147/IJN.S563711

For kinetic analysis, the cumulative DOX release at each temperature was first normalized to the equilibrium value at 24 h to obtain the fractional release $F = M_t/M_\infty$ (The cumulative DOX release at 24 h for that temperature is taken as M_∞, noted as equilibrium release, M_t refers to DOX release at the specific time). Only the initial data points with $F \leq 0.6$ were used, and these were fitted by linear regression to the zero-order model $F = kt$. As shown in Figure 9b, the early-stage release at 39, 41, and 43 °C exhibits excellent linearity, with apparent rate constants of 0.3835, 0.3747, and 0.3755 h^{-1} and correlation coefficients R^2=0.9948, 0.9978, and 0.9984, respectively. This indicates that once TD has melted, DOX release from CFO/Au-2/PAA/DOX/TD follows a pseudo-zero-order profile in the 0–60% region, and the release rate is only weakly dependent on temperature above the TD phase-transition point, consistent with diffusion-controlled liberation from an opened TD/PAA matrix.

Figure 9c demonstrates the controlled release performance under external stimuli, including NIR irradiation (laser), alternating magnetic field (AMF), and their combination. Minimal release is observed in the control group (no stimulus), while either NIR or AMF alone induces moderate release due to localized heating. Notably, the combination of NIR and AMF produces a combined effect, rapidly releasing over 50% of the encapsulated DOX within 6 hours, in a stepwise manner corresponding to the ON/OFF cycles of the stimuli. Under NIR and AMF stimulation, the suspension temperature exceeded 38 °C (as demonstrated in Figure 5b), triggering TD melting and enabling significant DOX release (Figure 9c). This confirms the thermally activated gating behavior of the TD layer.

The above results indicate that DOX release from CFO/Au-2/PAA/DOX/TD is controlled by a thermally triggered "gate-opening" mechanism. At 35–37 °C, TD remains in the solid state and, together with strong electrostatic/hydrogen-bond interactions between DOX and the PAA shell, effectively traps the drug inside the nanocomposite, leading to minimal cumulative release. Once the temperature exceeds the TD melting range (≈39–43 °C) or under NIR/AMF stimulation, TD melts and becomes permeable, and the hydrated PAA layer partially relaxes, which weakens DOX–PAA interactions. Consequently, DOX molecules can diffuse outward through the softened TD/PAA coating into the surrounding medium, giving a rapid, diffusion-controlled release after "switch-on" of the TD gate.

Figure 10a shows that CFO/Au-2/PAA/TD exhibits minimal cytotoxicity toward SW620 cells. Cell viability remains above 90% even at the highest tested carrier concentration (100 μg/mL), regardless of whether NIR + AMF stimulation is applied. This demonstrates that both the nanocarrier itself and hyperthermia alone have negligible cytotoxic effects toward SW620 cells. The cell-viability assays performed on SW620 cells serve to evaluate the therapeutic effect against colorectal cancer cells. Additional biocompatibility studies with normal cell lines will be carried out in future work to further assess the safety profile of the nanoplatform.

In contrast, Figure 10b reveals a strong dependence of cytotoxicity on external stimulation. CFO/Au-2/PAA/DOX/TD without NIR/AMF maintains high cell viability (>85%), confirming that the TD layer effectively blocks DOX release at physiological temperature. Under NIR + AMF, however, CFO/Au-2/PAA/DOX/TD causes a significant decrease in

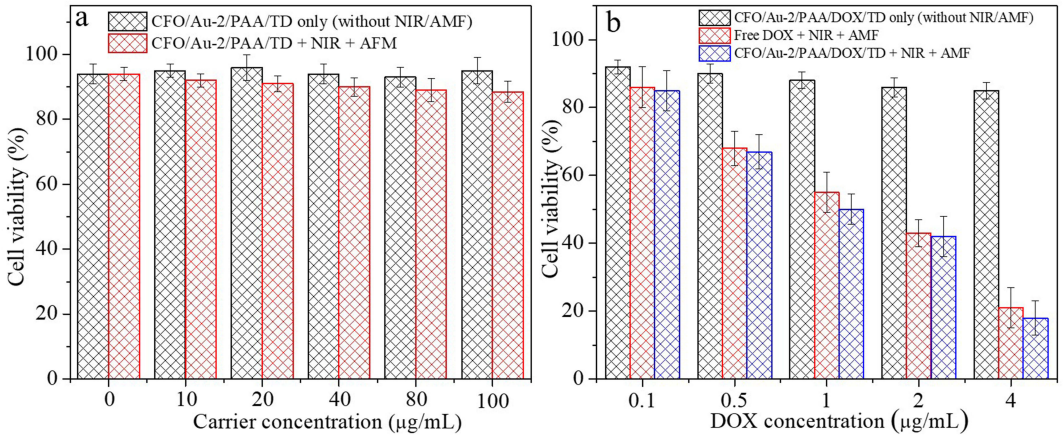

Figure 10 In vitro cytotoxicity assessment on SW620 cells: (**a**) Cell viability after treatment with CFO/Au-2/PAA/TD with/without NIR + AMF stimulation at different carrier concentrations. (**b**) Cell viability at different DOX concentrations for free DOX + NIR + AMF and CFO/Au-2/PAA/DOX/TD with/without NIR + AMF stimulation.

viability in a dose-dependent manner ($p < 0.05$), indicating efficient, stimuli-triggered DOX release. Notably, the dual-stimulus nanoplatform achieves a lower viability than free DOX at the same concentrations, demonstrating its superior therapeutic effect due to enhanced cellular uptake and localized drug delivery.

Collectively, these results confirm that the nanocarrier is intrinsically safe under normal physiological conditions, yet highly active upon dual-mode thermal activation, enabling precise control over chemotherapy while minimizing off-target toxicity.

While the MTT assay provides quantitative evidence of stimulus-dependent cytotoxicity, more detailed biological investigations such as live/dead fluorescence staining and apoptosis/necrosis analysis will be addressed in future studies to further elucidate the cell-death pathways induced by CFO/Au-2/PAA/DOX/TD.

Statistical comparisons were performed using one-way ANOVA ($p < 0.05$). In Figure 10a, no statistically significant difference in cell viability was observed among the CFO/Au-2/PAA/TD groups, either with or without NIR + AMF stimulation ($p > 0.05$), confirming the minimal cytotoxic contribution of hyperthermia alone. In contrast, Figure 10b shows that the viability of cells treated with CFO/Au-2/PAA/DOX/TD under NIR + AMF is lower than that of both the free DOX + NIR + AMF group and the non-stimulated nanocomposite group ($p < 0.05$), demonstrating that the improved anticancer efficacy originates from stimulus-triggered DOX release.

Conclusions

In this study, we successfully developed a multifunctional nanoplatform—CFO/Au-2/PAA/DOX/TD—for thermally gated and dual-stimuli-responsive drug delivery targeting colorectal cancer. $CoFe_2O_4$ nanocubes were uniformly coated with gold nanoparticles via atomic layer deposition, enabling strong photothermal conversion under NIR irradiation while retaining magnetic responsiveness for AMF-induced heating. Surface functionalization with poly(acrylic acid) (PAA) enhanced colloidal stability and facilitated efficient doxorubicin (DOX) loading. To prevent premature drug release, DOX was encapsulated with 1-tetradecanol (TD), a phase-change material that acts as a thermal gate, releasing the drug only upon heating above 38 °C.

The composite exhibited high DOX loading capacity (~26 wt%), excellent structural integrity, and strong thermal responsiveness. In vitro release studies demonstrated minimal DOX leakage at physiological temperatures and rapid release under NIR and/or AMF stimulation. Cytotoxicity assays against SW620 cells confirmed its enhanced therapeutic efficacy under dual-mode activation.

Overall, this nanoplatform integrates photothermal heating, and thermal-gated drug release in a single system, offering precise spatiotemporal control over drug delivery. These results demonstrate the feasibility of this ALD-engineered Au/CFO nanoplatform for dual-mode thermal activation and controlled DOX release in vitro, suggesting its potential for further development toward localized colorectal cancer therapy pending additional in-depth biological evaluation.

Disclosure

The authors report no conflicts of interest in this work.

References

1. Tian S, Chen M. Global research progress of nanomedicine and colorectal cancer: a bibliometrics and visualization analysis. *Front Oncol*. 2024;14:1460201. doi:10.3389/fonc.2024.1460201
2. Wang J, Wang H, Zou F, et al. The role of inorganic nanomaterials in overcoming challenges in colorectal cancer diagnosis and therapy. *Pharmaceutics*. 2025;17:4.
3. Noreen S, Maqbool I, Saleem A, Mahmood H, Rai N. Recent insights and applications of nanocarriers-based drug delivery systems for colonic drug delivery and cancer therapy: an updated review. *Crit Rev Oncol/Hematol*. 2025;208:104646. doi:10.1016/j.critrevonc.2025.104646
4. Radu ER, Semenescu A, Voicu SI. Recent advances in stimuli-responsive doxorubicin delivery systems for liver cancer therapy. *Polymers*. 2022;14 (23):5249. doi:10.3390/polym14235249
5. Chabner BA, Roberts TG. Chemotherapy and the war on cancer. *Nat Rev Cancer*. 2005;5(1):65–72. doi:10.1038/nrc1529
6. Tacar O, Sriamornsak P, Dass CR. Doxorubicin: an update on anticancer molecular action, toxicity and novel drug delivery systems. *J Pharm Pharmacol*. 2013;65(2):157–170. doi:10.1111/j.2042-7158.2012.01567.x
7. Nima ZA, Alwbari AM, Dantuluri V, et al. Targeting nano drug delivery to cancer cells using tunable, multi-layer, silver-decorated gold nanorods. *J Appl Toxicol*. 2017;37(12):1370–1378. doi:10.1002/jat.3495

8. Cheng H, Liao J, Ma Y, Sarwar MT, Yang H. Advances in targeted therapy for tumor with nanocarriers: a review. *Mater Today Bio*. 2025;31:101583. doi:10.1016/j.mtbio.2025.101583
9. Gressler S, Hipfinger C, Part F, Pavlicek A, Zafiu C, Giese B. A systematic review of nanocarriers used in medicine and beyond - definition and categorization framework. *J Nanobiotechnology*. 2025;23(1):90. doi:10.1186/s12951-025-03113-7
10. Arora K, Ledwani L, Komal. A comprehensive review on the synthesis and therapeutic potential of cobalt ferrite ($CoFe_2O_4$) nanoparticles. *ChemistrySelect*. 2025;10(1):e202404136. doi:10.1002/slct.202404136
11. Alves TEP, Pessoni HVS, Franco A, Burda C, Samia ACS. Magnetic-plasmonic properties of $CoFe_2O_4$@Au nanocomposite. *J Phys Chem Solids*. 2022;164:110630. doi:10.1016/j.jpcs.2022.110630
12. Singh JA, Yang N, Bent SF. Nanoengineering heterogeneous catalysts by atomic layer deposition. *Annu RevChem Biomol Eng*. 2017;8(1):41–62. doi:10.1146/annurev-chembioeng-060816-101547
13. Lines MG. Nanomaterials for practical functional uses. *J Alloy Compd*. 2008;449(1–2):242–245. doi:10.1016/j.jallcom.2006.02.082
14. Cheng N, Sun X. Single atom catalyst by atomic layer deposition technique. *Chin J Catal*. 2017;38(9):1508–1514. doi:10.1016/S1872-2067(17)62903-6
15. Pourmadadi M, Farokh A, Rahmani E, et al. Polyacrylic acid mediated targeted drug delivery nano-systems: a review. *J Drug Delivery Sci Technol*. 2023;80:104169. doi:10.1016/j.jddst.2023.104169
16. Vohl S, Ban I, Drofenik M, et al. Microwave synthesis of poly(acrylic) acid-coated magnetic nanoparticles as draw solutes in forward osmosis. *Materials*. 2023;16(11):4138. doi:10.3390/ma16114138
17. Arkaban H, Barani M, Akbarizadeh MR, et al. Polyacrylic acid nanoplatforms: antimicrobial, tissue engineering, and cancer theranostic applications. *Polymers*. 2022;14:6. doi:10.3390/polym14061259
18. Salimi M, Shokrgozar MA, Delavari H,H, Mehravi B, Vossoughi M. A temperature-responsive drug release system based on MoS2 nanosheets and 1-tetradecanol. *Colloids Surf A*. 2023;676:132061. doi:10.1016/j.colsurfa.2023.132061
19. Choi S-W, Zhang Y, Xia Y. A temperature-sensitive drug release system based on phase-change materials. *Angew Chem Int Ed*. 2010;49(43):7904–7908. doi:10.1002/anie.201004057
20. Bao J, Tu H, Li J, et al. Applications of phase change materials in smart drug delivery for cancer treatment. *Front Bioeng Biotechnol*. 2022;10:991005. doi:10.3389/fbioe.2022.991005
21. Zhang Z, Yuan Y, Zhang N, Cao X. Thermophysical properties of some fatty acids/surfactants as phase change slurries for thermal energy storage. *J Chem Eng Data*. 2015;60(8):2495–2501. doi:10.1021/acs.jced.5b00371
22. Xu X, Sun Y, Wang W, Ju L, Shu R, Gu H. An overview of polyethylene glycol composite phase change materials: preparation, physicochemical properties and application. *J Energy Storage*. 2024;104:114581. doi:10.1016/j.est.2024.114581
23. Motorzhina AV, Pshenichnikov SE, Anikin AA, et al. Gold/cobalt ferrite nanocomposite as a potential agent for photothermal therapy. *J Biophotonics*. 2024;17(7):e202300475. doi:10.1002/jbio.202300475
24. Chen BQ, Pan YJ, Zhang DG, Xia HY, Kankala RK. Phase-change materials-based platforms for biomedicine. *Front Bioeng Biotechnol*. 2022;10:989953. doi:10.3389/fbioe.2022.989953
25. He F, Chen Y, Li C, et al. Controllable drug release system based on phase change molecules as gatekeepers for bimodal tumor therapy with enhanced efficacy. *Rsc Adv*. 2016;6(70):65600–65606. doi:10.1039/C6RA10736B
26. Hussain A, Guo S. NIR-triggered release of DOX from sophorolipid-coated mesoporous carbon nanoparticles with the phase-change material 1-tetradecanol to treat MCF-7/ADR cells. *J Mat Chem B*. 2019;7(6):974–985. doi:10.1039/C8TB02673D
27. Huang X, Yu H, Tang G, Zhang S, Cai W, Chen L. Integration of iron phosphide onto CdIn2S4 accelerates carrier separation for efficient photocatalytic hydrogen evolution. *Inorg Chem Commun*. 2025;178:114552. doi:10.1016/j.inoche.2025.114552
28. Abu Serea ES, Orue I, García JÁ, Lanceros-Méndez S, Reguera J. Enhancement and tunability of plasmonic-magnetic hyperthermia through shape and size control of Au:Fe_3O_4 Janus nanoparticles. *ACS Appl Nano Mater*. 2023;6(19):18466–18479. doi:10.1021/acsanm.3c03818
29. García-García G, Lázaro M, Urquiza P, Romacho T, Delgado ÁV, Iglesias GR. Polydopamine coated nonspherical magnetic nanocluster for synergistic dual magneto-photothermal cancer therapy. *Polymers*. 2025;17(1):85. doi:10.3390/polym17010085
30. Muzzi B, Albino M, Gabbani A, et al. Star-shaped magnetic-plasmonic Au@Fe_3O_4 nano-heterostructures for photothermal therapy. *ACS Appl Mater Interfaces*. 2022;14:29087–29098. doi:10.1021/acsami.2c04865
31. Lázaro M, Delgado ÁV, Iglesias GR. Magneto-photothermal synergy applied to gold-coated magnetic nanoparticles. *J Magn Magn Mater*. 2024;591:171718. doi:10.1016/j.jmmm.2024.171718
32. Hashemi FSM, Grillo F, Ravikumar VR, et al. Thermal atomic layer deposition of gold nanoparticles: controlled growth and size selection for photocatalysis. *Nanoscale*. 2020;12(16):9005–9013. doi:10.1039/D0NR01092H
33. Muro-Cruces J, Roca AG, López-Ortega A, et al. Precise size control of the growth of Fe_3O_4 nanocubes over a wide size range using a rationally designed one-pot synthesis. *Acs Nano*. 2019;13(7):7716–7728. doi:10.1021/acsnano.9b01281
34. Saire-Saire S, Barbosa ECM, Garcia D, et al. Green synthesis of Au decorated $CoFe_2O_4$ nanoparticles for catalytic reduction of 4-nitrophenol and dimethylphenylsilane oxidation. *Rsc Adv*. 2019;9(38):22116–22123. doi:10.1039/C9RA04222A
35. Abbasi R, Nodehi A, Atai M. Synthesis of poly(acrylic-co-itaconic acid) through precipitation photopolymerization for glass-ionomer cements: characterization and properties of the cements. *Dent Mater*. 2020;36(6):e169–e183. doi:10.1016/j.dental.2020.03.006
36. Reddy MP, Mohamed AMA, Zhou XB, Du S, Huang Q. A facile hydrothermal synthesis, characterization and magnetic properties of mesoporous $CoFe_2O_4$ nanospheres. *J Magn Magn Mater*. 2015;388:40–44. doi:10.1016/j.jmmm.2015.04.009
37. Reindl M, Zach V, Schwaminger SP. Biocompatible Poly(acrylic acid-co-methacrylic acid)-coated iron oxide nanoparticles for enhanced adsorption and antimicrobial activity of Lasioglossin-III. *ACS Appl Mater Interfaces*. 2025;17(11):16644–16657. doi:10.1021/acsami.4c22603
38. Kim WJ, Lee EH, Kwon Y-J, Ye S-K, Kim KO. Targeted drug release system based on pH-responsive PAA-POSS nanoparticles. *RSC Adv*. 2022;12(28):18209–18214. doi:10.1039/D2RA01141G